

A non-intrusive reduced-order modeling method using polynomial chaos expansion

Xiang Sun^a, Xiaomin Pan^a, Jung-Il Choi^{a,*}

^a*Department of Computational Science and Engineering, Yonsei University, Seoul 03722, Republic of Korea*

Abstract

We propose a non-intrusive reduced-order modeling method based on proper orthogonal decomposition (POD) and polynomial chaos expansion (PCE) for stochastic representations in uncertainty quantification (UQ) analysis. Firstly, POD provides an optimally ordered basis from a set of selected full-order snapshots. Truncating this optimal basis, we then construct a reduced-order model with undetermined coefficients. Later, PCE is utilized to approximate the coefficients of the truncated basis. In this method, we construct a PCE using a non-intrusive regression-based method. Combined with the model reduction ability of POD, this makes the proposed method a powerful tool for stochastic representations in UQ analysis. To investigate the performance of the proposed method, we provide two numerical examples, i.e., a highly nonlinear analytical function with three uncertain parameters and a two-dimensional heat-driven cavity flow with a stochastic boundary temperature. The results demonstrate that the proposed method drastically reduces the computational costs and storage requirements that arise because of high-dimensional physical and random spaces. Further, it has comparable accuracy to that of the classical full-PCE in the predicting statistical quantities. In addition, it is able to reasonably predict the outputs of original high-fidelity models using only a few snapshots.

Keywords: Uncertainty quantification, Reduced-order modeling, Proper orthogonal decomposition, Polynomial chaos expansion

1. Introduction

Uncertainty quantification (UQ) is the process of quantifying the effects of input uncertainties on system responses. In recent years, UQ has been widely explored in many fields of science and engineering such as fluid [1, 2, 3] and structural mechanics [4, 5]. To reproduce the fine-scale structures of such physical phenomena, a large number of degree of freedom (DOF) for simulations is required, which clearly commensurates with increasing computational cost. Hence, for UQ, problems are in general too large to be tackled with standard techniques. This is because approximating system responses with large numbers of random parameters on a fine mesh is usually computationally challenging. This

*Corresponding author.

Email address: jic@yonsei.ac.kr (Jung-Il Choi)

emphasizes the need for establishing a model reduction method to reduce computational costs and storage requirements in UQ analysis of the problems with high-dimensional physical and random spaces.

A fundamental problem in UQ is approximating a computational model with random parameters. To this end, many numerical methods have been well developed in recent years (see [6, 7, 8, 9, 10, 11, 12] and references therein). One of the most widely used techniques in UQ is polynomial chaos expansion (PCE), which was first proposed by Ghanem and Spanos as finite-dimensional Wiener polynomial chaos [6, 13]. Later, Xiu and Karniadakis extended it to other random variables with basis functions from the Askey family of hypergeometric polynomials [14], which is known as generalized PCE. Further, PCE was extended for random variables with arbitrary distributions in [15, 16]. To obtain deterministic coefficients of the PCE, two kinds of approaches are used: intrusive and non-intrusive methods. Intrusive methods need solvers for the resulting coupled deterministic equations, which can be very complicated if the form of the equations is nontrivial and nonlinear. However, in the non-intrusive methods, existing solvers are taken as 'black box' without any modification of the underlying computer codes. The PCE methods always exhibit high convergence rates with increasing expansion order provided that solutions are sufficiently smooth with respect to the random variables. However, a well-known shortcoming of these methods is the "curse of dimensionality;" i.e., the simulation cost grows rapidly with increasing dimensions of random space. To mitigate this issue, various methods have been developed based on sampling strategies [17, 18, 19] and basis reduction [9, 12]. Nevertheless, for problems with high-dimensional physical space, constructing a PCE is still computationally challenging. This is because computational cost depends not only on the cost of the PCE construction, but also the number of spatial DOFs. Efficient reduced-order modeling (ROM) method are thus essential for such problems.

ROM [20] aims to approximate the original model using an accurate reduced-order model with a much smaller number of DOFs. Similar to PCE methods, ROM methods can be divided into two categories in terms of dependency on the governing equations: intrusive and non-intrusive [21]. Over the previous decades, many methods have been developed for ROMs (see [22, 23, 24] and references therein). In the present study, we focus on non-intrusive ROM methods based on POD [26]. Usually, POD-based ROM methods construct a set of basis functions from the snapshots of the original high-fidelity model and then approximate the model responses with these basis functions. To this end, a variety of methods have been introduced for POD-based ROM. Audouze et al. [25, 27] proposed a non-intrusive POD-based ROM using radial basis functions (RBFs) for approximating solutions of nonlinear time-dependent parameterized partial differential equations. Xiao et al. [28] proposed a non-intrusive ROM based on constrained POD and the Kriging interpolation method, where they used Kriging interpolation to compute the POD coefficients. Guo and Hesthaven [29, 30] approximated the POD coefficients using Gaussian process regression in ROMs for nonlinear structural analysis and time-dependent problems. Noack et al. [31] introduced neural networks for ROMs. Later, a non-intrusive ROM method based on POD and RBF artificial neural networks (ANN) was proposed by Vasile et al. [32]. Furthermore, ANNs, particularly multi-layer perceptrons, were introduced for ROMs to accurately approximate coefficients of the reduced model [33, 34]. Recently, a more extensive and comprehensive discussion on the use of machine learning for the approximation of POD coefficients was proposed in [35]. For more reviews of non-intrusive

POD based ROM methods, please refer to [24]. In the present study, we are interested in developing a non-intrusive ROM method for stochastic representations in UQ problems based on POD and PCE methods.

Recently, some algorithms have been proposed based on the POD and PCE methods (see [36, 37, 38, 39]). In [36], Doostan et al. proposed an intrusive stochastic model reduction method of creating an alternative optional basis for PCE bases by adapting the Karhunen-Lovève (KL) expansion [41]. More precisely, a stochastic basis was first obtained on a coarse mesh by means of a KL expansion of the coarse-scale response and then used as the basis functions in fine discretization analysis. According to the results of the numerical examples in [4] and [36], dramatic reduction of computational cost was achieved with little loss in accuracy. However, the method is intrusive, which may be very complicated or even impossible to implement in some cases. To mitigate this problem, Raise et al. [37, 38] extended this idea to a non-intrusive PCE method, which is more efficient and broadly applicable. Moreover, to further reduce the computational cost of PCE construction, Abraham et al. [39] further extended this non-intrusive method by introducing a sparse polynomial chaos expansion method [12]. Clearly, the new non-intrusive sparse PCE-based model reduction scheme brings a significant speed-up for a wide range of engineering problems, especially for those with high-dimensional random space. However, a full PCE still needs to be constructed on a coarse discretization, which is still a large computational challenge for some problems with high resolution in spatial discretization.

In this study, a non-intrusive ROM method is proposed for UQ problems with high-dimensional physical and random spaces. The method combines the advantages of both the POD and PCE methods. However, different to [40], where POD was first constructed from a data set of the ice shape as a reduced order model and then PCE was constructed based on this model to study the effects of uncertain parameters in POD representation. In our method, the POD basis is directly constructed for fine discretization using the method of snapshots [20]. Then, a sparse PCE method proposed in [9] is used to approximate the random coefficients of the POD representation. The method is referred as POD-PCE. To investigate the performance of this method, two numerical examples were tested: i.e., a highly irregular Ackley function with three random parameters and a two-dimensional heat-driven cavity flow with a stochastic boundary temperature. The results indicate the efficiency and accuracy of the POD-PCE in the representation of the stochastic field data computed from full order model with high spatial discretization and high random dimensionality. Moreover, similar to the classical PCE methods, the statistical quantities can be directly calculated from the deterministic coefficients and POD basis of the POD-PCE representation.

The rest of the paper is arranged as follows. In Section 2, we present the POD-PCE method for the representation of the stochastic field, where the construction of the POD basis based on the method of snapshots is shown, and a sparse PCE method is introduced to approximate the coefficients of the POD representation. Section 3 is dedicated to numerical tests of the POD-PCE method. Finally, in Section 4 we provide conclusions.

2. Representation of the random field

We consider a random-field model response $U(\mathbf{x}; \boldsymbol{\xi})$, where $\boldsymbol{\xi} = (\xi_1, \dots, \xi_d) \in \Gamma = \prod_{k=1}^d \Gamma_k \subset \mathbb{R}^d$ is a random vector with independent components described by the joint probability density function (PDF) $\rho(\boldsymbol{\xi}) = \prod_{k=1}^d \rho_k(\xi_k)$, where $\rho_k(\xi_k)$ is the PDF of the k -th component of the random vector. \mathbf{x} is a spatial vector varies in a compact set Ω of \mathbb{R}^s ($s = 1$ or 2 or 3). In the present study, we focus on the case of $s = 2$. Thus, variables \mathbf{x} are deterministic and vary on a grid of size N corresponding to a discretization of Ω . Therefore, $U(\mathbf{x}; \boldsymbol{\xi})$ is a N -dimensional output given by

$$\mathbf{U} = [U^{(1)}, U^{(2)}, \dots, U^{(N)}]^T, \quad (1)$$

Where $U^{(n)} = U(\mathbf{x}^{(n)}; \boldsymbol{\xi})$, $n = 1, 2, \dots, N$. Our objective is to develop a reduced-order model for $U(\mathbf{x}; \boldsymbol{\xi})$. The procedure of the construction of the reduced-order model is presented in the remainder of this section.

2.1. Proper orthogonal decomposition

We first consider a proper orthogonal decomposition (POD) method to build a reduced-order model. POD is a powerful and elegant method of data analysis aimed at deriving low-order models of dynamic systems. It was first proposed by Kosambi [26], and was widely used in various fields of engineering and science under a variety of different names such as Karhunen-Loève decomposition [41] in stochastic process modeling and principal component analysis in statistical analysis [42, 43]. The POD method essentially provides an optimally ordered orthonormal basis in the least-squares sense for a given set of theoretical, experimental, or computational data of high-dimensional systems [44]. The optimal lower-dimensional approximations for the given data are then obtained by truncating the optimal basis. In our work, the POD basis vectors are computed empirically using sampled data collected over a subset of the random space Ω_r , typically using the method of snapshots [20].

Consider an ensemble of snapshots, $\{\mathbf{U}_1, \mathbf{U}_2, \dots, \mathbf{U}_{N_s}\}$, where $\mathbf{U}_{n_s} \in \mathbb{R}^N$ denotes the n_s -th snapshot, and is given by

$$\mathbf{U}_{n_s} = [U_{n_s}^{(1)}, \dots, U_{n_s}^{(N)}]^T, \quad U_{n_s}^{(n)} = U(\mathbf{x}^{(n)}; \boldsymbol{\xi}^{(n_s)}), \quad n = 1, \dots, N, \quad n_s = 1, \dots, N_s. \quad (2)$$

Let $\mathbf{U} = [\mathbf{U}_1, \mathbf{U}_2, \dots, \mathbf{U}_{N_s}]$ be a real-valued snapshot matrix of rank $N_r \leq \min\{N, N_s\}$. Then, we have the following POD representation of $U(\mathbf{x}; \boldsymbol{\xi})$; i.e.,

$$U(\mathbf{x}; \boldsymbol{\xi}) \approx \sum_{l=1}^L u_l(\boldsymbol{\xi}) \psi_l(\mathbf{x}), \quad (3)$$

where $\psi_l(\mathbf{x})$ are the most characteristic structure functions extracted from the spatial domain Ω based on the snapshot matrix \mathbf{U} , $u_l(\boldsymbol{\xi})$ are the corresponding coefficients for a given random vector $\boldsymbol{\xi}$, and $L \in \{1, \dots, N_r\}$ is the number of selected structure functions. Therefore, the goal of the POD is to find a proper orthonormal basis $\{\psi_l\}_{l=1}^L$ ($\boldsymbol{\psi} = [\psi_l(\mathbf{x}^{(1)}), \dots, \psi_l(\mathbf{x}^{(N)})]^T$) of rank L for the given snapshots.

Since POD is usually reduced to the following eigenvalue problem

$$\mathcal{U}\mathcal{U}^T\psi = \lambda\psi, \quad (4)$$

it is strongly related to the singular value decomposition (SVD) [48] of matrix \mathcal{U} ; i.e.,

$$\mathcal{U} = \Psi\Sigma\mathbf{V}^T, \quad \Sigma = \begin{pmatrix} \mathbf{D} & \mathbf{0} \\ \mathbf{0} & \mathbf{0} \end{pmatrix}, \quad (5)$$

where $\mathbf{D} = \text{diagonal}(\sigma_1, \dots, \sigma_{N_r}) \in \mathbb{R}^{N_r \times N_r}$ containing the singular values $\sigma_1 \geq \sigma_2 \geq \dots \geq \sigma_{N_r} \geq 0$ and the zeros denote matrices of appropriate dimensions with zero-elements. $\Psi \in \mathbb{R}^{N \times N}$ and $\mathbf{V} \in \mathbb{R}^{N_s \times N_s}$ are unitary matrices, i.e., $\Psi\Psi^T = \Psi^T\Psi = \mathbf{I}_N$ and $\mathbf{V}\mathbf{V}^T = \mathbf{V}^T\mathbf{V} = \mathbf{I}_{N_s}$.

Let $\psi_{n_r} \in \mathbb{R}^N$ and $\nu_{n_r} \in \mathbb{R}^{N_s}$ be the n_r -th column vectors of Ψ and \mathbf{V} , respectively. Then we have

$$\mathcal{U}\nu_{n_r} = \sigma_{n_r}\psi_{n_r} \quad \text{and} \quad \mathcal{U}^T\psi_{n_r} = \sigma_{n_r}\nu_{n_r} \quad \text{for } n_r = 1, \dots, N_r. \quad (6)$$

Thus,

$$\mathcal{U}^T\mathcal{U}\nu_{n_r} = \sigma_{n_r}^2\nu_{n_r} \quad \text{and} \quad \mathcal{U}\mathcal{U}^T\psi_{n_r} = \sigma_{n_r}^2\psi_{n_r} \quad \text{for } n_r = 1, \dots, N_r. \quad (7)$$

Hence, $\{\psi_{n_r}\}_{n_r=1}^{N_r}$ and $\{\nu_{n_r}\}_{n_r=1}^{N_r}$ are eigenvectors of $\mathcal{U}\mathcal{U}^T$ and $\mathcal{U}^T\mathcal{U}$, respectively, with eigenvalues $\lambda_{n_r} = \sigma_{n_r}^2 > 0$, $n_r = 1, \dots, N_r$. In the present study, we assume that $N_s \ll N$. Therefore, rather than considering the eigenvalue problem (4), we consider the following eigenvalue problem

$$\mathcal{U}^T\mathcal{U}\nu = \lambda\nu. \quad (8)$$

According to Eq. (6), $\{\psi_l\}_{l=1}^L$ ($L \in \{1, \dots, N_r\}$, $\psi_l = \mathcal{U}\nu_l/\sqrt{\lambda_l}$) is the POD basis of rank L that we need [47]. Then, a reduced-order model is obtained by projecting the full order model onto the space spanned by the POD basis of rank L . The POD basis is optimal in the sense that it minimizes the least-squares error of the snapshot representation for the reduced basis of size L . Let $\tilde{\Psi} \in \mathbb{R}^{N \times L}$ be a matrix with pairwise orthonormal vector ψ_l . Then, the projection error of the snapshots can be evaluated as

$$\begin{aligned} \|\mathcal{U} - \tilde{\Psi}\tilde{\Psi}^T\mathcal{U}\|_F^2 &= \min_{\Psi^L \in \mathbb{R}^{N \times L}} \|\mathcal{U} - \Psi^L(\Psi^L)^T\mathcal{U}\|_F^2 \\ &= \min_{\Psi^L \in \mathbb{R}^{N \times L}} \sum_{n_s=1}^{N_s} \|\mathcal{U}_{n_s} - \Psi^L(\Psi^L)^T\mathcal{U}_{n_s}\|_2^2 = \sum_{n_s=L+1}^{N_s} \lambda_{n_s} = \sum_{n_s=L+1}^{N_r} \lambda_{n_s}, \end{aligned} \quad (9)$$

where $\Psi^L = [\psi_{l_1}, \dots, \psi_{l_L}]$ ($l_i \in \{1, \dots, N_r\}$, $i = 1, \dots, L$), $\|\cdot\|_2$ is the general L_2 norm for a vector (e.g., $\|\psi_l\|_2 = \sqrt{\sum_{n=1}^N \psi_l^2(\mathbf{x}^{(n)})}$), and $\|\cdot\|_F$ denotes the Frobenius norm given by

$$\|\mathbf{A}\|_F = \sqrt{\sum_{n_1=1}^{N_1} \sum_{n_2=1}^{N_2} |A_{n_1, n_2}|^2} \quad \text{for } \mathbf{A} \in \mathbb{R}^{N_1 \times N_2}. \quad (10)$$

From Eq. (9), one can see that the square of the error in the snapshot representation is given by the sum of the eigenvalues of the eigenvalue problem (8) corresponding to the modes not included in the selected basis. Furthermore, a fast decay of the eigenvalues of $\mathbf{U}^T \mathbf{U}$ is usually assumed in POD. Therefore, the size of the POD basis can be chosen by the size of the dominant eigenspace so that

$$\frac{\sum_{l=1}^L \lambda_l}{\sum_{l=1}^{N_r} \lambda_l} > 1 - \varepsilon, \quad (11)$$

where ε is a user-specified tolerance, often taken to be 10^{-3} or smaller [23]. The numerator of Eq. (11) is often referred to as the "energy" captured by the POD modes.

Let

$$V_N = \{U(\mathbf{x}; \boldsymbol{\xi}) : \mathbf{x} \in \Omega, \boldsymbol{\xi} \in \Gamma\}, \quad V_{N_s} = \text{span}\{\mathbf{U}_1, \mathbf{U}_2, \dots, \mathbf{U}_{N_s}\}, \quad \Xi = \text{span}\{\boldsymbol{\xi}^{(1)}, \boldsymbol{\xi}^{(2)}, \dots, \boldsymbol{\xi}^{(N_s)}\},$$

where V_N is the realization domain of $U(\mathbf{x}; \boldsymbol{\xi})$, $V_{N_s} \subset V_N$ is spanned by the snapshots and Ξ is a subset of Γ spanned by a set of selected random vectors. Then, if the random vectors are selected sufficiently well, $U(\mathbf{x}; \boldsymbol{\xi})$ can be approximated using the basis of V_{N_s} . As above-mentioned, the main result of POD is that the optimal subspace V_L of dimension $L \ll \min\{N, N_s\}$ representing the snapshots is given by $V_L = \text{span}\{\boldsymbol{\psi}_1, \boldsymbol{\psi}_2, \dots, \boldsymbol{\psi}_L\}$. Thus, for any random vector $\boldsymbol{\xi} \in \Gamma$, $U(\mathbf{x}; \boldsymbol{\xi})$ can be approximated as shown in Eq. (3). Clearly, the coefficients $u_l(\boldsymbol{\xi})$ in Eq. (3) vary with the random vector $\boldsymbol{\xi}$, which means that we can construct a mapping between the POD coefficients and the random vector $\boldsymbol{\xi}$. To this end, a sparse PCE method is introduced in the following subsection.

Remark 1. Note that the POD bases optimally approximate ensemble snapshots of field $U(\mathbf{x}; \boldsymbol{\xi})$ in the least-squares sense, but they are not bases approximating the field $U(\mathbf{x}; \boldsymbol{\xi})$. Only when the random vectors are selected well enough can the POD bases be used to approximate the field data. Hence, choosing good random vectors for the snapshots is important in the method of snapshots. In the present study, the snapshots are chosen by a sequential sampling scheme, as described in Section 2.4.

2.2. Polynomial chaos expansion

We now present the basic formulation of the stochastic representations of the coefficients $u_l(l = 1, \dots, L)$ in the POD representation of the random field $U(\mathbf{x}; \boldsymbol{\xi})$ using the PCE method.

The basic idea behind PCE is to use orthogonal polynomials in terms of random variables to approximate functions of those random variables. As shown in [8, 14], the polynomial basis $\phi^{(k)}(\xi_k)(k = 1, \dots, d)$ can be chosen on the basis of the correspondence between the weighting function of the polynomial family and the PDF of the random variable ξ_k ; for example, normal and uniform distributions correspond to Hermite and Legendre polynomial bases, respectively. Furthermore, the univariate polynomial bases $\phi^{(k)}(\xi_k)$ are satisfy the following orthogonality:

$$\mathbb{E} \left[\phi_i^{(k)}(\xi_k) \phi_j^{(k)}(\xi_k) \right] = \int_{\Gamma_k} \phi_i^{(k)}(\xi_k) \phi_j^{(k)}(\xi_k) \rho_k(\xi_k) d\xi_k = \delta_{ij}, \quad (12)$$

where δ_{ij} is the Kronecker delta function. Then, the PCE of $u_l(\boldsymbol{\xi})$ is defined as

$$u_l(\boldsymbol{\xi}) = \sum_{\boldsymbol{\alpha} \in \mathbb{N}^d} c_{\boldsymbol{\alpha}}^{(l)} \Phi_{\boldsymbol{\alpha}}(\boldsymbol{\xi}), \quad (13)$$

where $\Phi_{\boldsymbol{\alpha}}(\boldsymbol{\xi}) = \phi_{\alpha_1}^{(1)}(\xi_1) \cdots \phi_{\alpha_d}^{(d)}(\xi_d)$ are multivariate polynomials orthonormal with respect to $\rho(\boldsymbol{\xi})$ and $\boldsymbol{\alpha} \in \mathbb{N}^d$ is a multi-index that identifies the components of the multivariate polynomials $\Phi_{\boldsymbol{\alpha}}$ and satisfies that $|\boldsymbol{\alpha}| = \alpha_1 + \cdots + \alpha_d$, $|\boldsymbol{\alpha}| \geq 0$. In addition, $c_{\boldsymbol{\alpha}}^{(l)}$ are the deterministic coefficients corresponding to the polynomials. It is worth noting that the convergence of the Eq. (13) should be justified for different polynomials in practice. In short, Wiener-Hermite chaos [6] can be justified by the Cameron-Martin theorem [49]. More generally, rigorous justifications about the convergence of generalized PCE can be found in [50].

Practically, the sum in Eq. (13) needs to be truncated to a finite sum by introducing the truncated polynomial chaos expansion:

$$u_l(\boldsymbol{\xi}) \approx \sum_{\boldsymbol{\alpha} \in \mathcal{A}} c_{\boldsymbol{\alpha}}^{(l)} \Phi_{\boldsymbol{\alpha}}(\boldsymbol{\xi}), \quad (14)$$

where $\mathcal{A} \subset \mathbb{N}^d$ is the set of selected multi-indices of multivariate polynomials which may have the following form:

$$\mathcal{A} = \{\boldsymbol{\alpha} \in \mathbb{N}^d : |\boldsymbol{\alpha}| \leq p\}, \quad \text{card}\{\mathcal{A}\} = M = \frac{(p+d)!}{p!d!}. \quad (15)$$

Because of the orthogonality relations in Eq. (12), it follows that the multivariate polynomials are also orthonormal:

$$\mathbb{E} [\Phi_{\boldsymbol{\alpha}}(\boldsymbol{\xi}) \Phi_{\boldsymbol{\beta}}(\boldsymbol{\xi})] = \delta_{\boldsymbol{\alpha}\boldsymbol{\beta}}, \quad (16)$$

where $\delta_{\boldsymbol{\alpha}\boldsymbol{\beta}}$ is an extension Kronecker symbol to the multi-dimensional case. Based the orthogonality relations, we can easily estimate the statistical quantities of u_l , e.g., for a PCE with the first multivariate polynomial $\Phi_0(\boldsymbol{\xi}) = 1$, we have

$$\mu(u_l) = \mathbb{E} [u_l(\boldsymbol{\xi})] \approx \int_{\Gamma} \left(\sum_{\boldsymbol{\alpha} \in \mathcal{A}} c_{\boldsymbol{\alpha}}^{(l)} \Phi_{\boldsymbol{\alpha}}(\boldsymbol{\xi}) \right) \rho(\boldsymbol{\xi}) d\boldsymbol{\xi} = c_0^{(l)}, \quad (17)$$

and

$$\text{var}(u_l) = \mathbb{E} [(u_l(\boldsymbol{\xi}) - \mu(u_l))^2] \approx \sum_{0 < |\boldsymbol{\alpha}| \leq p} (c_{\boldsymbol{\alpha}}^{(l)})^2. \quad (18)$$

To calculate the coefficients of the PCE for a given polynomial basis, many methods have been proposed, e.g., see [8, 9, 51, 52, 53]. In the present study, only regression-based non-intrusive methods are considered, i.e., the PCE coefficients are estimated by minimizing the mean squared error of the response approximation. A direct approach to estimating the coefficients is to set up a least-squares minimization problem [54]. Thus, Eq. (13) can be written as a sum of its truncated version and a residual:

$$u_l(\boldsymbol{\xi}) = \sum_{m=0}^{M-1} c_m^{(l)} \Phi_m(\boldsymbol{\xi}) + \varepsilon_M = \boldsymbol{\Phi} \mathbf{c}^{(l)} + \varepsilon_M, \quad (19)$$

where ε_M is the truncation error, $\Phi = [\Phi_0(\xi), \dots, \Phi_{M-1}(\xi)]$ is the matrix that assembles the values of all the orthonormal polynomials in ξ , and $\mathbf{c}^{(l)} = [c_0^{(l)}, \dots, c_{M-1}^{(l)}]^T$ is a vector containing the coefficients.

The least-squares minimization problem is then set up as:

$$\hat{\mathbf{c}}^{(l)} = \arg \min_{\mathbf{c}^{(l)}} \mathbb{E} \left[\left(\Phi \mathbf{c}^{(l)} - u_l(\xi) \right)^2 \right]. \quad (20)$$

Given a sampling of size N_ξ of the random vector $\{\xi^{(n_\xi)}\}_{n_\xi=1}^{N_\xi}$, we have $\mathbf{U} = [U_1, U_2, \dots, U_{N_\xi}]$ ($N_s = N_\xi$). Based on Eq. (3), the corresponding coefficients can be estimated as $\mathbf{u}_l = \tilde{\Psi}^T \mathbf{U} = [u_l(\xi^{(1)}), \dots, u_l(\xi^{(N_\xi)})]^T$, then we have

$$\begin{aligned} \mathbb{E} \left[\left(\Phi \mathbf{c}^{(l)} - u_l(\xi) \right)^2 \right] &= \int_{\Gamma} \left(\Phi(\xi) \mathbf{c}^{(l)} - u_l(\xi) \right)^2 \rho(\xi) d\xi \\ &\approx \frac{1}{N_\xi} \sum_{n_\xi=1}^{N_\xi} \left(\Phi(\xi^{(n_\xi)}) \mathbf{c}^{(l)} - u_l(\xi^{(n_\xi)}) \right)^2 = \frac{1}{N_\xi} \|\mathbf{A} \mathbf{c}^{(l)} - \mathbf{u}_l\|_2^2. \end{aligned}$$

where

$$A_{n_\xi, m} = \Phi_m(\xi^{(n_\xi)}), \quad n_\xi = 1, \dots, N_\xi, \text{ and } m = 0, \dots, M-1. \quad (21)$$

Then, the ordinary least-square solution of Eq. (20) is calculated as:

$$\hat{\mathbf{c}}^{(l)} = (\mathbf{A}^T \mathbf{A})^{-1} \mathbf{A}^T \mathbf{u}_l. \quad (22)$$

According to Hosder et al. [52], $2M \sim 3M$ samples are sufficient for accurate approximation to the statistics at each polynomial degree. However, considering this experimental design, the computational effort may become untenable for large values of d or p , e.g., $d \geq 10$ or $p \geq 10$. To mitigate this issue, several methods have been developed (see [9, 12, 55] and references therein). In our work, the least-angle regression-based adaptive sparse PCE is adopted, which is developed based on the sparsity of effects, i.e., that most computational models are driven by main effects and low-order interactions [9]. In fact, the sparse PCE solves a modified least-squares problem in Eq. (23) by adding a penalty term:

$$\hat{\mathbf{c}}^{(l)} = \arg \min_{\mathbf{c}^{(l)}} \mathbb{E} \left[\left(\Phi \mathbf{c}^{(l)} - u_l(\xi) \right)^2 \right] + \gamma \|\mathbf{c}^{(l)}\|_1, \quad (23)$$

where γ is the regularization parameter and $\|\cdot\|_1$ is the l_1 norm that sums the absolute element of a vector.

Remark 2. Note that conventional PCE methods focus on the problem with smooth model response with regard to input variables. Thus when there are steep gradient or finite discontinuities in the random space, these methods converge very slowly or even fail to converge due to a linear combination of polynomials. For these cases, local expansions may be more efficient than expansions with global polynomials, such as the wavelet expansions [56] and the multi-element generalized PCE [57, 58]. In the present study, we mainly focus on the problems with smooth responses with respect to input variables.

2.3. POD-PCE

Combining the POD representation (Eq. (3)) and the PCE approximations (Eq. (14)) of the undetermined coefficients of the POD basis, a whole representation of the random field $U(\mathbf{x}; \boldsymbol{\xi})$ is obtained as follows:

$$U(\mathbf{x}; \boldsymbol{\xi}) \approx \tilde{U}(\mathbf{x}; \boldsymbol{\xi}) = \sum_{l=1}^L \left(\sum_{m=0}^{M-1} c_m^{(l)} \Phi_m(\boldsymbol{\xi}) \right) \psi_l(\mathbf{x}). \quad (24)$$

This stochastic representation is referred as POD-PCE in the present study. The method reduces the spatial dimensionality from N to L . Furthermore, similarly to the classical PCE methods, it can estimate the statistical quantities of $U(\mathbf{x}; \boldsymbol{\xi})$ in terms of $\boldsymbol{\xi}$ using the orthogonality of the PCE; more precisely, the statistical quantities can be calculated by PCE coefficients and POD basis functions; e.g.,

$$\mu(U(\mathbf{x}; \boldsymbol{\xi})) = \mathbb{E}[U(\mathbf{x}; \boldsymbol{\xi})] \approx \mathbb{E} \left[\sum_{l=1}^L u_l(\boldsymbol{\xi}) \psi_l(\mathbf{x}) \right] = \sum_{l=1}^L \mathbb{E}[u_l(\boldsymbol{\xi})] \psi_l(\mathbf{x}) = \sum_{l=1}^L c_0^{(l)} \psi_l(\mathbf{x}), \quad (25)$$

and

$$\text{var}(U(\mathbf{x}; \boldsymbol{\xi})) \approx \text{var} \left[\sum_{l=1}^L u_l(\boldsymbol{\xi}) \psi_l(\mathbf{x}) \right] = \sum_{l_1=1}^L \sum_{l_2=1}^L \psi_{l_1}(\mathbf{x}) \psi_{l_2}(\mathbf{x}) \text{Cov}(u_{l_1}, u_{l_2}), \quad (26)$$

where

$$\text{Cov}(u_{l_1}, u_{l_2}) = \mathbb{E}[(u_{l_1}(\boldsymbol{\xi}) - \mu(u_{l_1}))(u_{l_2}(\boldsymbol{\xi}) - \mu(u_{l_2}))] \quad (27)$$

$$\approx \mathbb{E}[(u_{l_1}(\boldsymbol{\xi}) - c_0^{(l_1)})(u_{l_2}(\boldsymbol{\xi}) - c_0^{(l_2)})] \quad (28)$$

$$= \sum_{m=1}^{M-1} c_m^{(l_1)} c_m^{(l_2)}, \quad (29)$$

and $\text{var}(u_l)$ is calculated as shown in Eq. (18).

2.4. Design of experiment in POD-PCE

As presented in the above subsections, a good design of experiment (DoE) is necessary in both POD and PCE parts. In the POD parts, we have to generate a proper set of snapshots such that the POD basis extracted from these snapshots is able to be used to approximate the random field response. In PCE part, a proper number of random samples should be generated to obtain a convergent results under some accuracy requirements.

According to the discussion in [47], the continuous form of the eigenvalue problem (8) can be written as:

$$\int_{\Gamma} \langle \mathbf{U}, \boldsymbol{\psi} \rangle_{\mathbb{R}^N} U(\mathbf{x}; \boldsymbol{\xi}) \rho(\boldsymbol{\xi}) d\boldsymbol{\xi} = \lambda \psi(\mathbf{x}). \quad (30)$$

where $\langle \cdot, \cdot \rangle_{\mathbb{R}^N}$ is the inner product in \mathbb{R}^N and $\langle \mathbf{U}, \boldsymbol{\psi} \rangle_{\mathbb{R}^N} = \mathbf{U}^T \boldsymbol{\psi}$. Then, we have

$$\sum_{n_1=1}^N \left(\int_{\Gamma} U(\mathbf{x}^{(n_1)}; \boldsymbol{\xi}) U(\mathbf{x}^{(n_2)}; \boldsymbol{\xi}) \rho(\boldsymbol{\xi}) d\boldsymbol{\xi} \right) \psi(\mathbf{x}^{(n_1)}) = \lambda \psi(\mathbf{x}^{(n_2)}), \quad n_2 = 1, \dots, N. \quad (31)$$

Let

$$C_{n_1, n_2} = \int_{\Gamma} U(\mathbf{x}^{(n_1)}; \boldsymbol{\xi}) U(\mathbf{x}^{(n_2)}; \boldsymbol{\xi}) \rho(\boldsymbol{\xi}) d\boldsymbol{\xi} = \mathbb{E} \left[U(\mathbf{x}^{(n_1)}; \boldsymbol{\xi}) U(\mathbf{x}^{(n_2)}; \boldsymbol{\xi}) \right], \quad n_1 = 1, \dots, N, \quad n_2 = 1, \dots, N. \quad (32)$$

We obtain the following eigenvalue problem:

$$\mathbf{C}\boldsymbol{\psi} = \lambda\boldsymbol{\psi}, \quad (33)$$

where $\mathbf{C} = (C_{n_1, n_2})_{N \times N}$ is the correlation matrix of random field $U(\mathbf{x}; \boldsymbol{\xi})$. Compared to the eigenvalue problem (4), $\mathbf{U}\mathbf{U}^T$ can be thought of as an approximation to \mathbf{C} . The approximation accuracy depends on the method used to solve Eq. (32), such as Latin Hypercube sampling method [7], Sparse Grid [59] and greedy sampling method [60]. In the present study, we approximate \mathbf{C} by using the snapshots chosen by a sequential sampling scheme as follows:

1. Generate an initial set of random vectors as $\boldsymbol{\Theta}_0 = \{\boldsymbol{\xi}^{(1)}, \dots, \boldsymbol{\xi}^{(N_0)}\}$ using the Latin hypercube sampling (LHS) method [7];
2. Calculate snapshots \mathbf{U}_{n_0} ($n_0 = 1, \dots, N_0$) and assemble the snapshot matrix $\mathbf{U} = [\mathbf{U}_1, \dots, \mathbf{U}_{N_0}]$;
3. Solve the eigenvalue problem of $\mathbf{U}^T \mathbf{U}$ to generate $\lambda_{n_0}^0$ and normalize the eigenvalues as $\hat{\lambda}_{n_0}^0 = \frac{\lambda_{n_0}^0}{\lambda_1^0}$, $\lambda_1^0 \geq \dots \geq \lambda_{N_0}^0$;
4. Enrich $\boldsymbol{\Theta}_0$ to be $\boldsymbol{\Theta}_1 \supset \boldsymbol{\Theta}_0$ of size N_1 using a nested LHS method [45] and repeat (2)–(3) to obtain normalized eigenvalues $\{\hat{\lambda}_{n_1}^1\}_{n_1=1}^{N_1}$;
5. Select N_l eigenvalues such that $\hat{\lambda}_{N_l}^k > \tau$, $k = 0, 1$ and compute the mean absolute relative error as $\varepsilon_\lambda = \frac{1}{N_l} \sum_{n_l=1}^{N_l} \left| \frac{\hat{\lambda}_{n_l}^0 - \hat{\lambda}_{n_l}^1}{\hat{\lambda}_{n_l}^1} \right|$;
6. Update $\boldsymbol{\Theta}_0 = \boldsymbol{\Theta}_1$, $N_0 = N_1$ and repeat (1)–(5) until $\varepsilon_\lambda < \hat{\tau}$. Then define the number of the snapshots as $N_s = N_0$ and select $\mathcal{D}_{POD} = \{(\boldsymbol{\xi}^{(n_s)}, \mathbf{U}_{n_s}), n_s = 1, 2, \dots, N_s\}$ as the DoE of the POD construction.

In the above procedure, tolerance τ is used to select the eigenvalues with large "energy". Because the decay of eigenvalue is usually very fast and under some value, the eigenvalue has tiny influence on the total energy. The tolerance can be used to reduce the computation complexity of error ε_λ . For the tolerance $\hat{\tau}$, it is the stopping criterion of the procedure which ensures that the difference between the eigenvalues computed by the neighbour iterations is small enough. In the present study, we set $\tau = 10^{-10}$ and $\hat{\tau} = 0.05$ throughout the paper.

For the PCE part, the DoE is defined as $\mathcal{D}_{PCE} = \left\{ \left(\boldsymbol{\xi}^{(n_s)}, \tilde{\Psi}^T \mathbf{U}(\boldsymbol{\xi}^{(n_s)}) \right), n_s = 1, 2, \dots, N_s \right\}$ (see Section 2.2). This means that we use the same size DoE for both POD and PCE. It is first because that we apply sparse PCE to approximate the coefficients of POD which can obtain an accurate approximation by only a few samples of input variables. Second, the above snapshot selection procedure shows that the final selected snapshots lead to a set of convergent normalized eigenvalues. This means that the eigenvalue has same decay when we have N_s or more than N_s snapshots. Thus, the N_s snapshots are able to capture the most of information of the random field $U(\mathbf{x}; \boldsymbol{\xi})$. Therefore,

using the same DoE in PCE is reasonable. In case of that the PCE approximation does not satisfy the accuracy requirement under the same DoE with POD, we can enrich the samples using the nested LHS.

2.5. Error analysis

For any given parameters $\boldsymbol{\xi} \in \Gamma$, we have

$$\begin{aligned} U(\boldsymbol{x}; \boldsymbol{\xi}) &= \sum_{l=1}^L \left(\sum_{m=0}^{M-1} c_m^{(l)} \Phi_m(\boldsymbol{\xi}) + \varepsilon_M^{(l)} \right) \psi_l(\boldsymbol{x}) + \varepsilon_L(\boldsymbol{x}) \\ &= \sum_{l=1}^L \sum_{m=0}^{M-1} c_m^{(l)} \Phi_m(\boldsymbol{\xi}) \psi_l(\boldsymbol{x}) + \sum_{l=1}^L \varepsilon_M^{(l)} \psi_l(\boldsymbol{x}) + \varepsilon_L(\boldsymbol{x}). \end{aligned} \quad (34)$$

where $\varepsilon_L(\boldsymbol{x})$ is the error caused by POD truncation and snapshot selection. Let $\boldsymbol{\varepsilon}_M = [\varepsilon_M^{(1)}, \dots, \varepsilon_M^{(L)}]$ and $\boldsymbol{\varepsilon}_L = [\varepsilon_L(\boldsymbol{x}^{(1)}), \dots, \varepsilon_L(\boldsymbol{x}^{(N)})]$. Then, the error of POD-PCE approximation to $U(\boldsymbol{x}; \boldsymbol{\xi})$ for a spatial discretization of N grids is defined as follows

$$\begin{aligned} \varepsilon_{PP} &= \left\| \boldsymbol{U} - \tilde{\boldsymbol{U}} \right\|_2 = \left\| \tilde{\boldsymbol{\Psi}} \boldsymbol{\varepsilon}_M + \boldsymbol{\varepsilon}_L \right\|_2 \\ &\leq \left\| \tilde{\boldsymbol{\Psi}} \boldsymbol{\varepsilon}_M \right\|_2 + \left\| \boldsymbol{\varepsilon}_L \right\|_2 \\ &\leq \left\| \tilde{\boldsymbol{\Psi}} \right\|_{2,2} \left\| \boldsymbol{\varepsilon}_M \right\|_2 + \left\| \left(\boldsymbol{U} - \hat{\boldsymbol{\Psi}} \hat{\boldsymbol{\Psi}}^T \boldsymbol{U} \right) + \left(\hat{\boldsymbol{\Psi}} \hat{\boldsymbol{\Psi}}^T \boldsymbol{U} - \tilde{\boldsymbol{\Psi}} \tilde{\boldsymbol{\Psi}}^T \boldsymbol{U} \right) \right\|_2 \\ &\leq \left\| \tilde{\boldsymbol{\Psi}} \right\|_{2,2} \left\| \boldsymbol{\varepsilon}_M \right\|_2 + \left\| \boldsymbol{U} - \hat{\boldsymbol{\Psi}} \hat{\boldsymbol{\Psi}}^T \boldsymbol{U} \right\|_2 + \left\| \hat{\boldsymbol{\Psi}} \hat{\boldsymbol{\Psi}}^T \boldsymbol{U} - \tilde{\boldsymbol{\Psi}} \tilde{\boldsymbol{\Psi}}^T \boldsymbol{U} \right\|_2 \\ &\leq \varepsilon_{PCE} + \varepsilon_{ss} + \varepsilon_{rb}, \end{aligned} \quad (35)$$

where $\hat{\boldsymbol{\Psi}} \hat{\boldsymbol{\Psi}}^T$ is the continuous covariance matrix of the random field, which has the form of Eq. (32), and $\|\cdot\|_{2,2}$ is an matrix norm induced by L_2 norm, e.g.,

$$\left\| \tilde{\boldsymbol{\Psi}} \right\|_{2,2} = \sup_{\boldsymbol{y} \neq \mathbf{0}} \frac{\left\| \tilde{\boldsymbol{\Psi}} \boldsymbol{y} \right\|_2}{\left\| \boldsymbol{y} \right\|_2}, \boldsymbol{y} \in \mathbb{R}^L.$$

Since $\tilde{\boldsymbol{\Psi}} \tilde{\boldsymbol{\Psi}}^T = \boldsymbol{I}_N$, $\left\| \tilde{\boldsymbol{\Psi}} \right\|_{2,2} = 1$. Then we have

$$\begin{aligned} \varepsilon_{PCE} &= \left\| \tilde{\boldsymbol{\Psi}} \right\|_{2,2} \left\| \boldsymbol{\varepsilon}_M \right\|_2 = \left\| \boldsymbol{\varepsilon}_M \right\|_2, \\ \varepsilon_{rb} &= \left\| \boldsymbol{U} - \hat{\boldsymbol{\Psi}} \hat{\boldsymbol{\Psi}}^T \boldsymbol{U} \right\|_2 \leq \sqrt{\lambda_{L+1}}, \\ \varepsilon_{ss} &= \left\| \hat{\boldsymbol{\Psi}} \hat{\boldsymbol{\Psi}}^T \boldsymbol{U} - \tilde{\boldsymbol{\Psi}} \tilde{\boldsymbol{\Psi}}^T \boldsymbol{U} \right\|_2 \leq \left\| \hat{\boldsymbol{\Psi}} \hat{\boldsymbol{\Psi}}^T - \tilde{\boldsymbol{\Psi}} \tilde{\boldsymbol{\Psi}}^T \right\|_{2,2} \left\| \boldsymbol{U} \right\|_2 = \tilde{C} \left\| \tilde{\boldsymbol{\Psi}} \tilde{\boldsymbol{\Psi}}^T \right\|_{2,2} \left\| \boldsymbol{U} \right\|_2 = \tilde{C} \left\| \boldsymbol{U} \right\|_2, \end{aligned} \quad (36)$$

where \tilde{C} is a constant related to the methods for the snapshot selection, e.g., $\tilde{C} \sim O(N_s^{-1/2})$ for standard Monte Carlo methods [61] and $\tilde{C} \sim O((N_s)^{-k} (\log N_s)^{(d-1)(k+1)})$ for the Smolyak sparse-grid method [62]. Therefore, ε_{ss} depends on the number of snapshots. As discussed in Section 2.1, ε_{rb} depends on a user-specified tolerance ε ; i.e., ε_{rb} decreases as ε decreases. For ε_{PCE} , it depends on the maximum order p and the size of DoE (N_ξ) [8]. In the present study, the snapshots are chosen using a sequential sampling scheme as shown in Section 2.4. The PCE construction uses a non-intrusive regression-based method as proposed in [9]. Hence, the accuracy of POD-PCE depends on the number of the snapshots (N_s), the tolerance ε , the maximum polynomial order (p) and the size of DoE (N_ξ).

2.6. Implementation of POD-PCE

In this section, we summarize the overall procedure of constructing a POD-PCE representation for a \mathbb{R}^N -valued random field $U(\mathbf{x}; \boldsymbol{\xi})$. To construct a POD-PCE, we first choose a set of snapshots using a sequential sampling method as shown in Section 2.4. Second, we construct the POD basis using the selected snapshots and obtain a set of reduced basis in the following steps:

1. Assemble the snapshot matrix $\mathbf{U} = [\mathbf{U}_1, \dots, \mathbf{U}_{N_s}]$ and solve the eigenvalue problem of $\mathbf{U}^T \mathbf{U}$ by Eq. (8) to generate λ_{n_s} and $\boldsymbol{\nu}_{n_s}$, $n_s = 1, 2, \dots, N_s$;
2. Set $\boldsymbol{\psi}_{n_r} = \frac{\mathbf{U} \boldsymbol{\nu}_{n_r}}{\sqrt{\lambda_{n_r}}}$, $n_r = 1, 2, \dots, N_r$;
3. Reduce the basis to be $\{\boldsymbol{\psi}_l\}_{l=1}^L$ such that condition (11) is satisfied.
4. Define the reduced POD basis matrix as $\tilde{\boldsymbol{\Psi}} = [\boldsymbol{\psi}_1, \boldsymbol{\psi}_2, \dots, \boldsymbol{\psi}_L]$.

Third, a sparse PCE method is utilized to approximate the undetermined coefficients of POD:

1. Prepare the DoE as $\{(\boldsymbol{\xi}^{(n_s)}, u_l(\boldsymbol{\xi}^{(n_s)}))\}$, $n_s = 1, 2, \dots, N_s$;
2. Select a set of orthogonal polynomials corresponding to the distribution of the random variables.
3. Construct the PCEs of $u_l(\boldsymbol{\xi})$ as Eq. (13) by solving the l_1 minimization problem (23).

Finally, a POD-PCE representation of $U(\mathbf{x}; \boldsymbol{\xi})$ is constructed using Eq. (24).

It should be noted that all the PCE constructions in this paper are done by using the least angle regression algorithm with UQLab [63].

3. Numerical examples

3.1. Highly irregular Ackley function

First, we consider a highly irregular Ackley function with three random parameters. The formulation of this function is given by

$$u(\mathbf{x}; \boldsymbol{\xi}) = -20(1 + 0.1\xi_3) \left(\exp \left[-0.2(1 + 0.1\xi_2) \sqrt{0.5(x^2 + y^2)} \right] \right) \quad (37)$$

$$- \exp(0.5[\cos(2\pi(1 + 0.1\xi_1)x) + \cos(2\pi(1 + 0.1\xi_1)y)]) + 20 + e, \quad (38)$$

where $\boldsymbol{\xi} = [\xi_1, \xi_2, \xi_3]$ is a random vector with independent components that are uniformly distributed over $[-1, 1]^3$.

According to the discussion in [37], a discretization with 400×400 nodes is needed to reproduce the fine-scale structures of the deterministic Ackley function. Hence, such a fine mesh is adopted in the present study for UQ analysis of the stochastic Ackley function. Figure 1 shows the Ackley function on the mesh for a randomly generated parameter vector, where the structure of the function is well depicted.

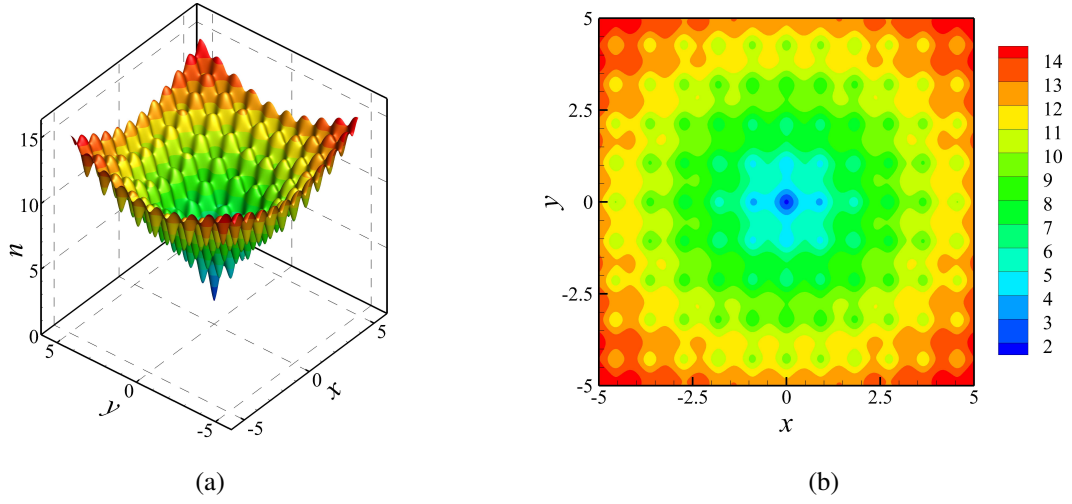


Figure 1: A realization of the random field $u(\mathbf{x}, \xi)$: (a) 3D plot and (b) contour plot.

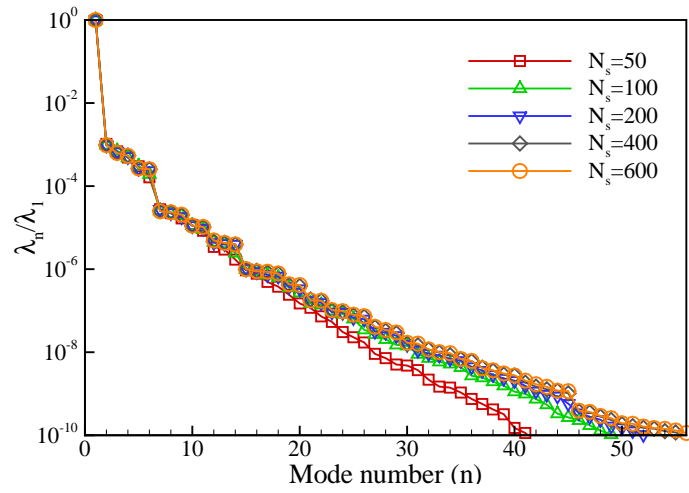


Figure 2: Normalized eigenvalues calculated using different numbers of snapshots for the stochastic Ackley function.

As discussed in Section 2, to construct a POD-PCE representation, a proper set of snapshots of a size of $N_s = 400$ was first selected by following the procedure in Section 2.4. Figure 2 shows the normalized eigenvalues calculated using different numbers of snapshots in the snapshot selection procedure. We observe that there is a sharp drop in the first seven eigenvalues. This indicates that most of the information in $u(\mathbf{x}; \boldsymbol{\xi})$ can be captured using the first seven modes. This is confirmed from Table 1, where the result shows that the first seven modes capture 99.99% of the total energy.

With the selected snapshots and the corresponding random vectors, we constructed both POD-PCE and full PCE (FPCE) for the output field data of the stochastic Ackley function. Similar to the PCE construction for the POD coefficients in Section 2.2, the full PCE of $u(\mathbf{x}; \boldsymbol{\xi})$ is constructed as follows:

$$u(\mathbf{x}; \boldsymbol{\xi}) \approx \sum_{\alpha \in \mathcal{A}} c_{\alpha}(\mathbf{x}) \Phi_{\alpha}(\boldsymbol{\xi}). \quad (39)$$

The maximum order of the polynomials in the PCE construction parts was set as $p = 13$ according to the recommendation in [37]. Furthermore, Monte Carlo (MC) simulations were performed using 3×10^3 LHS samples in order to validate the accuracy of POD-PCE. Given $N_s = 400$, we investigated the accuracy of POD-PCE in the prediction of statistical quantities by changing the value of ε . The results are shown in Table 1, where the number of the selected POD bases (L) and the mean absolute relative errors (MAREs) in mean and variance predictions are presented for different values of ε . The MAREs between POD-PCE and full PCE are defined as follows:

$$\varepsilon_{r,\mu}^{FPCE} = \frac{1}{N} \sum_{i=1}^N \left| \frac{\mu_{POD-PCE}(i) - \mu_{FPCE}(i)}{\mu_{FPCE}(i)} \right|, \quad \varepsilon_{r,var}^{FPCE} = \frac{1}{N} \sum_{i=1}^N \left| \frac{var_{POD-PCE}(i) - var_{FPCE}(i)}{var_{FPCE}(i)} \right|. \quad (40)$$

Similar definitions can be obtained for the MAREs between POD-PCE and MC; i.e., $\varepsilon_{r,\mu}^{MC}$ and $\varepsilon_{r,var}^{MC}$. It is seen that the MAREs between POD-PCE and MC (or full PCE) in mean and variance predictions decrease and the number of the selected POD bases increases as the value of ε decreases from $\varepsilon = 10^{-4}$ to $\varepsilon = 10^{-8}$. Furthermore, the decreasing tendency is tending to flat as ε becomes smaller. In particular, when $\varepsilon \leq 10^{-8}$, the MAREs between POD-PCE and MC are nearly unchanged and the MAREs between POD-PCE and full PCE are also very small. This indicates that POD-PCE and PCE have almost the same accuracy in mean and variance predictions. However, it is worth noting that POD-PCE only needs to construct 40 PCEs for the undetermined coefficients of the selected POD bases for $\varepsilon = 10^{-8}$, while full PCE needs to construct $N = 160000$ PCEs for the whole field data. Clearly, an enormous amount computational cost is reduced by using POD-PCE method. This because that same PCE algorithm with same parameter setting is used for PCE constructions in both POD-PCE and full PCE. In summary, POD-PCE constructed based on $\varepsilon = 10^{-8}$ is able to predict mean and variance with similar accuracy to that of the classical full PCE at a much cheaper cost.

Next, we considered the effects of the number of snapshots (N_s) on the accuracy of POD-PCE in predicting statistical quantities for the tolerance $\varepsilon = 10^{-8}$. We are interested in investigating whether the POD-PCE constructed using small number of snapshots can provide estimations of statistical quantities as reasonable as those obtained using

Tolerance	Size of selected POD basis	MARE in mean		MARE in variance	
ε	L	$\varepsilon_{r,\mu}^{MC}$	$\varepsilon_{r,\mu}^{FPCE}$	$\varepsilon_{r,var}^{MC}$	$\varepsilon_{r,var}^{FPCE}$
10^{-4}	7	2.4695E-04	2.4117E-04	1.8000E-02	1.6200E-02
10^{-5}	13	6.0376E-05	5.4439E-05	5.4000E-03	2.3000E-03
10^{-6}	20	2.6024E-05	1.7988E-05	4.5000E-03	6.7358E-04
10^{-7}	29	1.9915E-05	1.0626E-05	4.3000E-03	2.5562E-04
10^{-8}	40	1.6268E-05	3.2476E-06	4.3000E-03	1.1670E-04
10^{-9}	52	1.6278E-05	2.3119E-06	4.3000E-03	7.7865E-05

Table 1: Effects of ε on L and MAREs in mean and variance predictions for $N_s = 400$ for the stochastic Ackley function.

No. of snapshots	Size of selected POD basis	MARE in mean	MARE in variance
N_s	L	$\varepsilon_{r,\mu}^{FPCE}$	$\varepsilon_{r,var}^{FPCE}$
50	31	6.2769E-04	3.1000E-02
100	37	2.0937E-04	4.0000E-03
200	39	4.0501E-05	9.0066E-03
400	40	3.2476E-06	1.1670E-04
600	41	2.6858E-06	9.7453E-05

Table 2: Effects of N_s on L and MAREs in mean and variance predictions for $\varepsilon = 10^{-8}$ for the stochastic Ackley function.

the classical full PCE method. Table 2 shows the effects of N_s on the size of the selected POD basis and MAREs in mean and variance predictions for the stochastic Ackley function. POD-PCE results approach to the results of full PCE as the number of snapshots increases. Furthermore, we observe that even the POD-PCE constructed using 50 snapshots can predict the mean and variance with reasonable accuracy. However, the error in variance prediction is always larger than that in mean prediction, which implies that higher order moment prediction requires higher accuracy PCE, a attention should be paid on the high order moment prediction in PCE construction.

Finally, the efficiency and accuracy of the method of snapshots is validated by the comparison of eigenvalues calculated using full PCE and the method of snapshots. In the method of snapshots, eigenvalues are calculated using 400 snapshots by Eq. (8). For the full PCE method, the eigenvalues are obtained by solving the eigenvalue problem of the correlation matrix $\mathbf{R} = (r_{n_1, n_2})_{N \times N}$ with

$$r_{n_1, n_2} = \sum_{m=1}^{M-1} c_m(\mathbf{x}^{(n_1)})c_m(\mathbf{x}^{(n_2)}), \quad n_1 = 1, 2, \dots, N, \quad n_2 = 1, 2, \dots, N, \quad (41)$$

where $c_k(\mathbf{x}^{(\cdot)})$ are deterministic coefficients of Eq. (39) corresponding to grid $\mathbf{x}^{(\cdot)}$. The comparison result is shown in Figure 3, where we only present eigenvalues corresponding to the modes truncated by the tolerance $\varepsilon = 10^{-8}$. For the full PCE method, 42 bases are selected, which is slightly larger than that in the method of snapshots. However, the comparison shows good agreement for almost all eigenvalues. Only tiny discrepancies exist in the calculation of the smallest eigenvalues. Therefore, the method of snapshots is accurate enough to be used to construct the POD basis

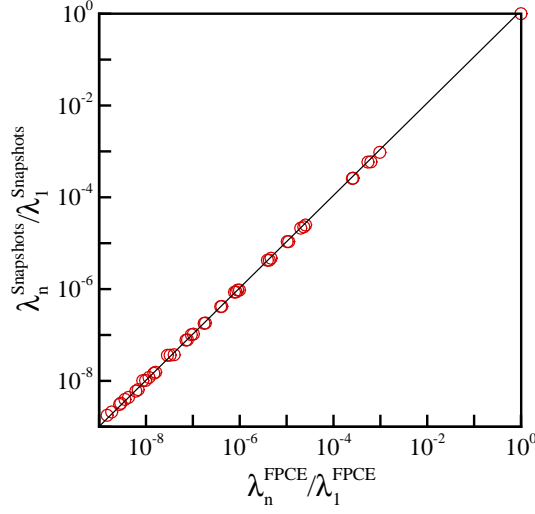


Figure 3: A comparison of the eigenvalues calculated from the full PCE and the method of snapshots.

compared with the methods discussed in [36, 37, 39].

3.2. Heat-driven cavity flow with a stochastic boundary temperature

To further investigate the performance of the proposed POD-PCE method, we consider a thermally driven cavity flow with stochastic boundary temperatures in a square domain, which is widely used as an numerical example in the validation of UQ algorithms (see [64, 65, 66] and references therein). Figure 4 shows the schematic of the problem with the computational domain, boundary conditions, and a realization of the stochastic temperature field. As described in [65, 66], the boundary temperature T_h on the left vertical wall is uniform, while the boundary temperature $T_c < T_h$ on the right vertical wall is a spatially varying random field. In terms of dimensionless variables, the time-dependent governing equations for fluids are presented as follows:

$$\frac{\partial \mathbf{u}}{\partial t} + \mathbf{u} \cdot \nabla \mathbf{u} = -\nabla p + \frac{Pr}{\sqrt{Ra}} \nabla^2 \mathbf{u} + Pr T \mathbf{e}_y, \quad (42)$$

$$\nabla \cdot \mathbf{u} = 0, \quad (43)$$

$$\frac{\partial T}{\partial t} + \nabla \cdot (\mathbf{u} T) = \frac{1}{\sqrt{Ra}} \nabla^2 T, \quad (44)$$

where \mathbf{u} , p , and T are the velocity vector, pressure, and temperature, respectively. \mathbf{e}_y denotes the unit normal vector in the vertical dimension. The dimensionless variables employed in the governing equations are defined as follows:

$$x = \frac{\tilde{x}}{L}, \quad y = \frac{\tilde{y}}{L}, \quad u_i = \frac{\tilde{u}_i}{U_0}, \quad t = \frac{\tilde{t}}{L/U_0}, \quad p = \frac{\tilde{p}}{\rho U_0^2}, \quad T = \frac{\tilde{T} - (T_h + \bar{T}_c)/2}{T_h - \bar{T}_c},$$

$$Pr = \frac{\nu}{\alpha}, \quad Ra = \frac{g\beta(T_h - \bar{T}_c)L^3}{\nu\alpha},$$

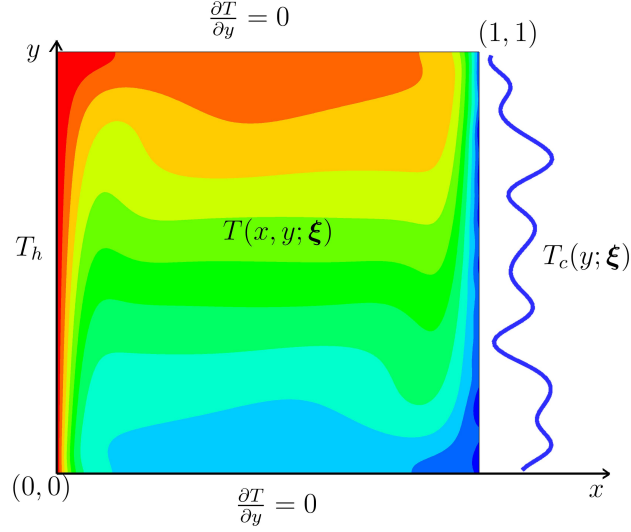


Figure 4: Illustration of the problem: computational domain, boundary conditions, and a realization of the stochastic temperature field.

where x (and y), $L = 1$, u_i , $U_0 = \sqrt{g\beta L(T_h - \bar{T}_c)\alpha/\nu}$, T_h , and \bar{T}_c respectively represent the Cartesian coordinates, characteristic length, velocity components, characteristic velocity, hot wall temperature, and cold wall mean temperature. In addition, α , $\beta = 0.5$, ν , ρ , and g respectively represent the thermal diffusivity, thermal expansion coefficient, kinematic viscosity, fluid density, and gravitational acceleration. The symbol \sim indicates a dimensional variable. Here, the Prandtl and Rayleigh numbers are set to $Pr = 0.71$ and $Ra = 10^6$.

The temperature on the hot wall is set to a constant value, i.e., $T_h = 0.5$. On the cold wall, we consider a boundary temperature with stochastic fluctuations as follows:

$$T_c(x = 1, y) = \bar{T}_c + T'_c(y), \quad (45)$$

where $\bar{T}_c = -0.5$ is a constant mean temperature and $T'_c(y)$ is the random component, which can be expressed in a truncated Karhunen-Loève expansion as described in [65, 66]:

$$T'_c(y, \xi) = \sigma_T \sum_{i=1}^d \sqrt{\lambda_i} \psi_i(y) \xi_i, \quad (46)$$

where ξ_i are uniform random variables assumed to be independently and uniformly distributed over $[-1, 1]$ and λ_i and $\psi_i(y)$ are the eigenvalues and eigenfunctions of the exponential correlation function

$$C(y_1, y_2) = \sigma_T^2 \exp\left(-\frac{|y_1 - y_2|}{l}\right), \quad (47)$$

with $\sigma_T = 11/100$ and $l = 1/21$. Here, $d = 20$ means that only largest eigenvalues and the corresponding eigenfunctions are kept to be used to represent the random field $T'_c(y)$ with the random variables ξ_i .

By Eqs. (45) and (46), deterministic boundary temperatures on the cold wall can be obtained for any random vector $\xi = [\xi_1, \dots, \xi_d]$. Then, computations are performed using the deterministic monolithic projection method developed in

No. of grid nodes	Averaged Nusselt number (\overline{Nu})	Relative difference
32×32	11.3216	28.2306%
64×64	9.2967	5.2970%
128×128	8.9193	1.0218%
256×256	8.84401	0.1698%
512×512	8.82901	–

Table 3: Grid convergence analysis based on averaged Nusselt number on the hot wall.

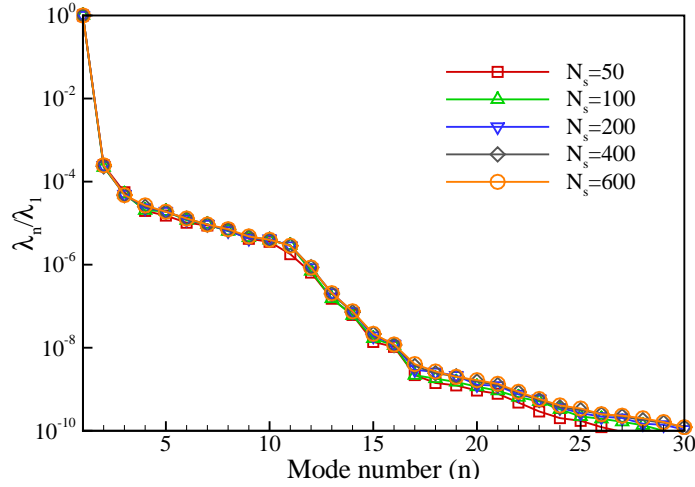


Figure 5: Eigenvalues calculated for different numbers of snapshots for the stochastic heat-driven cavity flow problem.

[67, 68, 69]. In this problem, a fine mesh is found by performing grid convergence analysis on the averaged Nusselt number \overline{Nu} on the hot wall for meshes with 32×32 , 64×64 , 128×128 , 256×256 , and 513×513 grid nodes. \overline{Nu} is obtained by integrating the local Nusselt number $Nu = -(\partial T / \partial x)|_{x=0}$ along the hot wall. The results are shown in Table 3. Finally, we chose the mesh with 256×256 grid nodes as the fine mesh because it featured the smallest and most reasonable relative difference from the mesh with 513×513 grid nodes. To investigate the performance of POD-PCE, the output temperature field denoted by $T(\mathbf{x}; \boldsymbol{\xi})$ was considered in this numerical test.

Similarly to the former example, the size of the snapshots was first chosen as $n_s = 400$ using the sequential sampling scheme described in Section 2.4. Figure 5 presents all the normalized eigenvalues calculated by the considered snapshots in decreasing order. Compared to the stochastic Ackley function problem, the current calculated eigenvalues decay much more quickly. Furthermore, we observed a sharp drop in the first three eigenvalues, which means that the first three modes capture most of the information in the temperature field.

Having obtained the reduced POD basis with $N_s = 400$ snapshots, PCEs are constructed with $p = 4$ for both POD-PCE and full PCE for $T(\mathbf{x}; \boldsymbol{\xi})$. The maximum order of polynomials is chosen as that in [65], where a good performance of a sparse PCE with $p = 4$ is shown in the representation of the stochastic solutions of Eqs. (42)–(44). It should be noted that the fourth-order classical full PCE is constructed using 400 snapshots and their corresponding

Tolerance	Size of selected POD basis	MARE in mean	MARE in variance
ε	L	$\varepsilon_{r,\mu}^{FPCE}$	$\varepsilon_{r,var}^{FPCE}$
10^{-4}	3	8.5751E-05	1.6665
10^{-5}	9	9.0676E-05	2.4500E-2
10^{-6}	12	9.0842E-05	1.3300E-02
10^{-7}	14	3.0573E-05	5.6000E-03
10^{-8}	18	2.5137E-05	5.4000E-03
10^{-9}	28	2.3924E-05	5.4000E-03

Table 4: Effects of ε on L and MAREs in mean and variance predictions for $N_s = 400$ in the stochastic heat-driven cavity flow problem.

No. of snapshots	Size of selected POD basis	MARE in mean	MARE in variance
N_s	L	$\varepsilon_{r,\mu}^{FPCE}$	$\varepsilon_{r,var}^{FPCE}$
50	16	2.2670E-05	7.9990E-01
100	17	2.8925E-05	3.9400E-02
200	18	1.5711E-05	7.4000E-03
400	18	2.2587E-06	5.4000E-03
600	18	4.1937E-06	5.2000E-03

Table 5: Effects of N_s on L and MAREs in mean and variance predictions for $\varepsilon = 10^{-8}$ for the stochastic heat-driven cavity flow problem.

random vectors throughout this example. The effects of ε and N_s on the accuracy of POD-PCE in the prediction of statistical quantities are shown in Tables 4 and 5, respectively. Similarly to the previous example, there is a good agreement between POD-PCE results and full PCE results. In particular, the MAREs in mean predictions are very small, even for a large tolerance or less snapshots. This is because the first mode is the mean. Thus, as long as the first mode is selected, we can give a reasonable and accurate estimate of the mean value. For the MAREs in variance predictions, both ε and N_s have positive effects in that the MAREs decrease with decreasing ε or increasing N_s and finally almost the same variance predictions can be obtained by POD-PCE to those of full PCE. These indicate that POD-PCE has a similar accuracy to the classical full PCE in the predictions of statistical quantities of $T(\mathbf{x}; \boldsymbol{\xi})$. Furthermore, it can reasonably predict the statistical quantities with less snapshots; e.g, using snapshots of size $N_s = 100$. In addition, one can find that the MARE of mean prediction increases when $N_s = 600$. This is because that the larger input samples improve the accuracy of POD-PCE, while the full PCE only used 400 input samples, the MARE therefore becomes larger compared to the case of $N_s = 400$. In fact, the mean prediction is gradually convergent as N_s increases. This is illustrated in Table 6, where $\varepsilon_{r,\mu}^{1000}$ and $\varepsilon_{r,var}^{1000}$ denotes the MAREs computed based on the case of $N_s = 1000$.

To further investigate the accuracy of POD-PCE, we first compared the prediction results of POD-PCE and full PCE for a realization of $T(\mathbf{x}; \boldsymbol{\xi})$. The results are shown in Figure 6 with the result directly simulated from Eqs. (42)–(44). We observe that the contours of temperature fields are almost the same, and it is difficult to distinguish differences among these contour plots. This indicates that both full PCE and POD-PCE can give an accurate prediction of $T(\mathbf{x}; \boldsymbol{\xi})$.

No. of snapshots	Size of selected POD basis	MARE in mean	MARE in variance
N_s	L	$\varepsilon_{r,\mu}^{1000}$	$\varepsilon_{r,var}^{1000}$
200	18	3.1563E-05	2.4200E-02
400	18	7.1596E-06	6.1000E-03
600	18	3.8645E-06	1.5000E-03
800	18	2.6028E-06	7.9285E-04
1000	18	—	—

Table 6: MAREs in mean and variance predictions for $\varepsilon = 10^{-8}$ for different number of snapshots compared with the case of $N_s = 1000$.

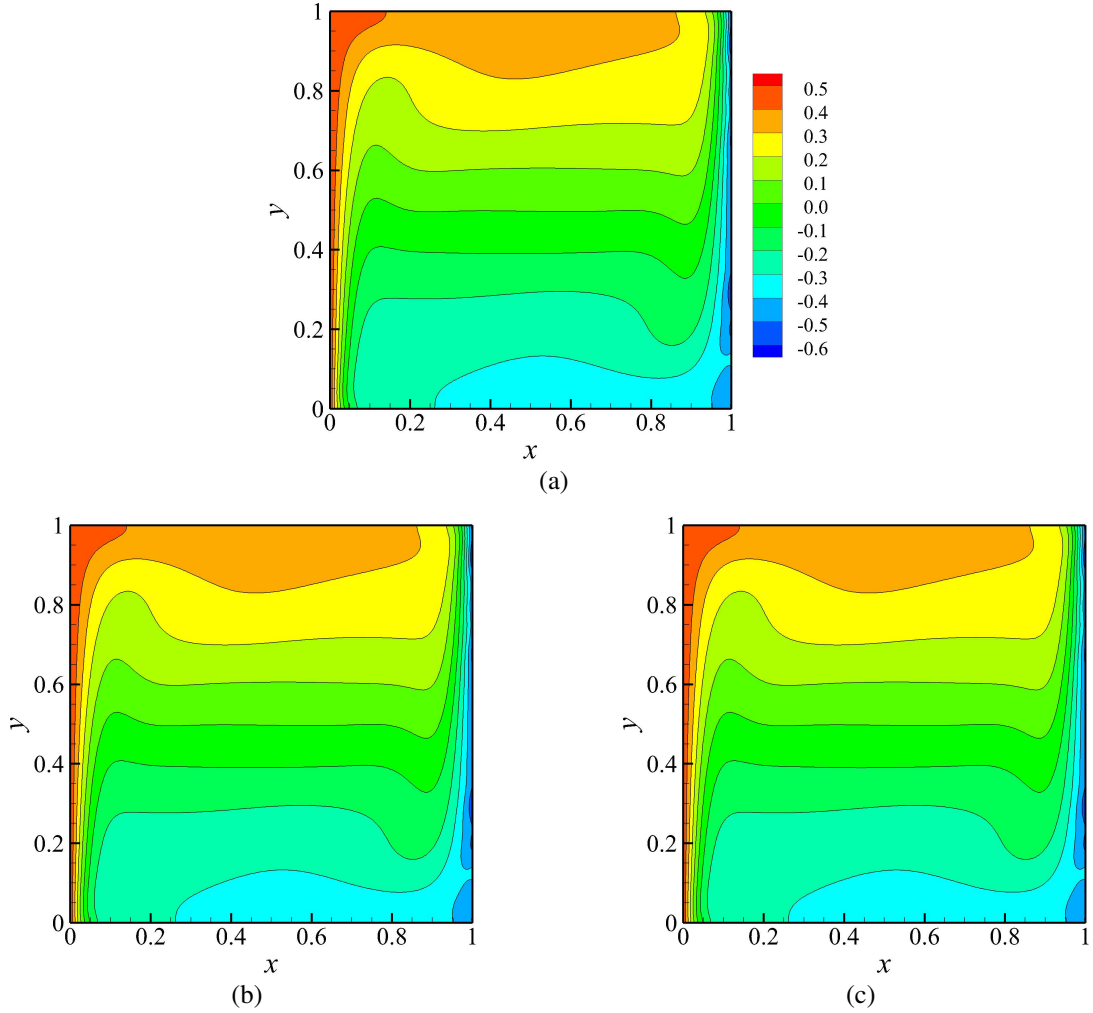


Figure 6: $T(\mathbf{x}; \boldsymbol{\xi})$ for one randomly generated boundary temperature on the cold wall calculated by: (a) direct simulation of the full order model, (b) POD-PCE, and (c) full PCE.

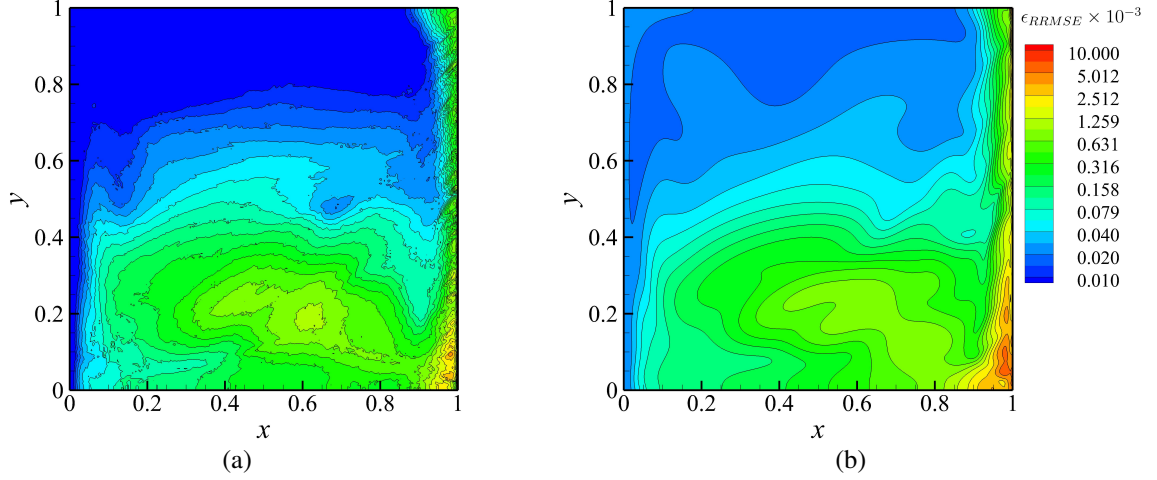


Figure 7: Distributions of RRMSE for the predictions of $T(\mathbf{x}; \boldsymbol{\xi})$ in : (a) full PCE and (b) POD-PCE. Two cases are performed based on 100 randomly generated boundary temperatures on the cold wall.

and the errors in the full PCE and POD-PCE predictions are comparable. However, we guess that some larger errors in the predictions of POD-PCE and full PCE may exist near the right cold wall due to the uncertain temperature boundary condition.

Next, we measured the error in the predictions of POD-PCE and full PCE by relative root mean-squared error (RRMSE), defined by

$$\varepsilon_{RRMSE}(\mathbf{x}) = \frac{\sqrt{\frac{1}{N_s} \sum_{n_s=1}^{N_s} (T_{LF}(\mathbf{x}; \boldsymbol{\xi}^{(n_s)}) - T_{HF}(\mathbf{x}; \boldsymbol{\xi}^{(n_s)}))^2}}{\sqrt{\frac{1}{N_s} \sum_{n_s=1}^{N_s} T_{HF}(\mathbf{x}; \boldsymbol{\xi}^{(n_s)})^2}}, \quad (48)$$

where HF denotes the high-fidelity result directly simulated from the cfull order model and LF represents the low-fidelity result estimated from POD-PCE or full PCE. The results are shown in Figure 7, where we compare the distributions of RRMSE for the predictions of $T(\mathbf{x}; \boldsymbol{\xi})$ in POD-PCE and full PCE. The RRMSEs are computed based on 100 realizations of $T(\mathbf{x}; \boldsymbol{\xi})$ calculated via direct simulation, POD-PCE, and full PCE for 100 randomly generated input variable vectors $\{\boldsymbol{\xi}^k\}_{k=1}^{100}$. It is found that large RRMSEs are mainly distributed near the right cold wall, especially at the right bottom angle of the computational domain. Furthermore, larger RRMSEs exist in the predictions of POD-PCE compared to those in full PCE. This is because of the error introduced by the truncated POD in POD-PCE method. In fact, these larger RRMSEs may tend to the values of the corresponding RRMSEs of the full PCE when we decrease the selection tolerance, which can be illustrated in Figure 8(b). In addition, we can find that the values of RRMSE of POD-PCE and full PCE are comparable in the predictions of $T(\mathbf{x}; \boldsymbol{\xi})$. This indicates that the POD-PCE has a comparable accuracy to full PCE in the prediction of $T(\mathbf{x}; \boldsymbol{\xi})$.

Finally, we investigate the effects of the number of snapshots (N_s) and the tolerance (ε) of POD basis selection on the accuracy of POD-PCE using the averaged RRMSEs over the temperature field. By Eq. (48), the averaged RRMSEs

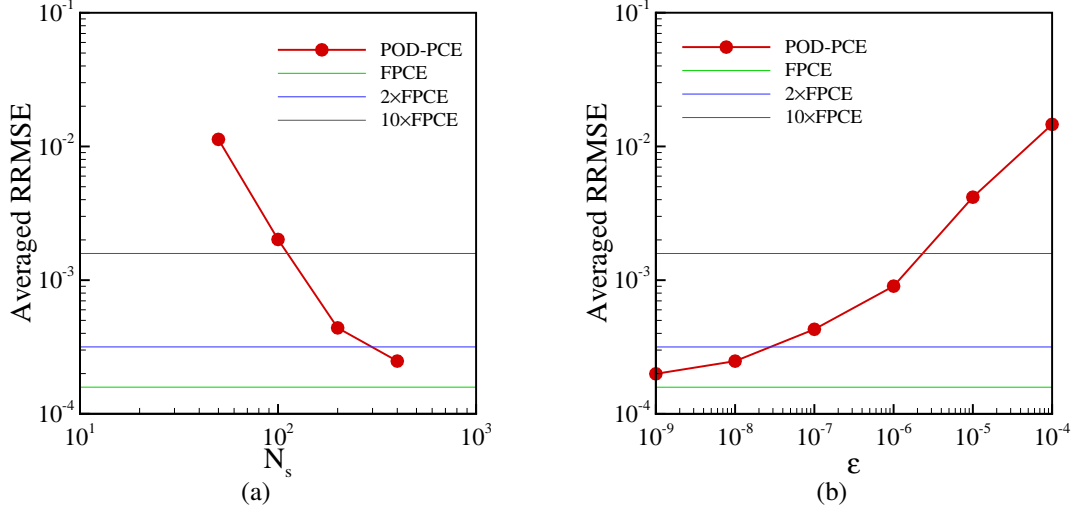


Figure 8: Averaged RRMSE of $T(\mathbf{x}; \boldsymbol{\xi})$ predictions using the POD-PCE method as a function of (a) snapshots size and (b) size of selected POD basis. All results are calculated based on 100 randomly generated boundary temperatures on the cold wall.

are given by

$$\hat{\varepsilon}_{RRMSE} = \frac{1}{N} \sum_{n=1}^N \varepsilon_{RMSE}(\mathbf{x}^{(n)}). \quad (49)$$

For a fixed tolerance $\varepsilon = 10^{-8}$, the averaged RRMSEs of $T(\mathbf{x}; \boldsymbol{\xi})$ predictions in the POD-PCE method are calculated for the aforementioned 100 realizations for different N_s . The results are shown in Figure 8(a). The error decreases with the increasing number of snapshots. However, the error decreasing rate becomes smaller at the same time, which is similar to the results shown in Table 5. In summary, when $N_s > 100$, POD-PCE has a comparable averaged RRMSE to that of full PCE and when $N_s > 200$ and close to 400, a similar averaged RRMSE can be obtained. It should be noted that the difference between two average RRMSEs at $N_s = 400$ is mainly coming from the POD truncation. Therefore, one can decrease the value of the tolerance of the POD basis selection to improve the accuracy of POD-PCE. This is studied in Figure 8(b), where the averaged RRMSEs are computed for a fixed number of snapshots, i.e., $N_s = 400$. Clearly, we observe that the error decreases as ε decreases. Similarly, when the value of the tolerance reaches some threshold, the error decreasing rate becomes smaller. Furthermore, we find that, when $\varepsilon \leq 10^{-8}$, POD-PCE can have similar averaged RRMSE to that of full PCE. In summary, if we use the same expansion order in the PCE construction parts for both POD-PCE and full PCE, the accuracy of POD-PCE depends on N_s and ε . By properly choosing the number of snapshots and the tolerance value, the proposed POD-PCE method can deliver similar accuracy to that of the classical full PCE method. In this example, POD-PCE with $N_s = 400$ and $\varepsilon = 10^{-8}$ is sufficient to obtain similar accuracy to that of the full PCE method in the prediction of $T(\mathbf{x}, \boldsymbol{\xi})$ and its statistical quantities.

4. Conclusion

We developed a non-intrusive reduced-order modeling method for the stochastic representations in uncertainty quantification analysis of problems with high-dimensional physical and random spaces. The method is based on a model reduction technique named proper orthogonal decomposition (POD) and an efficient stochastic spectral method, namely polynomial chaos expansion (PCE). POD is used to extract a set of reduced basis functions from a data ensemble collected from the full order model, i.e., snapshots. PCE is used to approximate the undetermined coefficients of the reduced basis. In particular, a non-intrusive sparse PCE is used to deal with highly random dimensionality problems. The proposed method inherits advantages of both POD and PCE methods. It can provide a reduced-order representation over the physical space as well as efficiently estimating the statistical quantities without increased computational cost. Two examples were tested to investigate the performance of the proposed method, i.e., an analytic highly irregular Ackley function with three random parameters and a heat-driven cavity flow with a stochastic boundary temperature. The results show that the proposed method is able to reduce the model order from properly chosen snapshots at a reasonable accuracy. Furthermore, under the same parameter setting for the PCE construction, the proposed method can predict the model response and its statistical quantities with a comparable accuracy to that of the classical full PCE method at a much cheaper cost. This implies great potential for the proposed method applied in uncertainty quantification analysis.

5. Acknowledgements

This work was supported by the National Research Foundation of Korea(NRF) grant funded by the Korea government(Ministry of Science and ICT) (NRF-2017R1E1A1A0-3070161 and NRF-20151009350).

References

- [1] H. N. Najm, Uncertainty quantification and polynomial chaos techniques in computational fluid dynamics, *Annu. Rev. Fluid Mech.* 41 (1) (2009) 35–52.
- [2] O. Le Maître, O. M. Knio, *Spectral methods for uncertainty quantification: with applications to computational fluid dynamics*, Springer Science & Business Media, 2010.
- [3] X. Sun, J. Park, J.-I. Choi, G. H. Rhee, Uncertainty quantification of upstream wind effects on single-sided ventilation in a building using generalized polynomial chaos method, *Build. Environ.* 125 (2017) 153–167.
- [4] R. Ghanem, G. Saad, A. Doostan, Efficient solution of stochastic systems: application to the embankment dam problem, *Struct. Saf.* 29 (3) (2007) 238–251.
- [5] G. I. Schueller, On the treatment of uncertainties in structural mechanics and analysis, *Comput. Struct.* 85 (5–6) (2007) 235–243.
- [6] R. G. Ghanem, P. D. Spanos, *Stochastic finite elements: A spectral approach*, Springer Verlag, New York, 1991.
- [7] J. Helton, F. Davis, Latin hypercube sampling and the propagation of uncertainty in analyses of complex systems, *Reliab. Eng. Syst. Safe.* 81 (1) (2003) 23–69.
- [8] D. B. Xiu, *Numerical methods for stochastic computations: a spectral method approach*, Princeton university press, 2010.

- [9] G. Blatman, B. Sudret, Adaptive sparse polynomial chaos expansion based on Least Angle Regression, *J. Comput. Phys.* 230 (6) (2011) 2345–2367.
- [10] V. Yadav, S. Rahman, Adaptive-sparse polynomial dimensional decomposition methods for high-dimensional stochastic computing, *Comput. Methods Appl. Mech. Eng.* 274 (2014) 56–83.
- [11] R. Schobi, B. Sudret, J. Wiart, Polynomial-chaos-based Kriging. *Int. J. Uncertain. Quantif.* 5 (2) (2015) 171–193.
- [12] S. Abraham, M. Raisee, G. Ghorbaniasl, F. Contino, C. Lacor, A robust and efficient stepwise regression method for building sparse polynomial chaos expansions, *J. Comput. Phys.* 332 (2017) 461–474.
- [13] N. Wiener, The homogeneous chaos, *Amer. J. Math.* 60 (1938) 897–936.
- [14] D. B. Xiu, G.E. Karniadakis, The Wiener-Askey polynomial chaos for stochastic differential equations, *SIAM J. Sci. Comput.* 24 (2) (2002) 619–644.
- [15] J. A. S. Witteveen, S. Sarkar, H. Bijl, Modeling physical uncertainties in dynamic stall induced fluid-structure interaction of turbine blades using arbitrary polynomial chaos, *Comput. Struct.* 85 (2007) 866–878.
- [16] S. Oladyshkin, W. Nowak, Data-driven uncertainty quantification using the arbitrary polynomial chaos expansion. *Reliab. Eng. Syst. Safe.* 1 (106) (2012) 179–190.
- [17] D. Xiu, J. S. Hesthaven, High-order collocation methods for differential equations with random inputs. *SIAM J. Sci. Comput.* 27 (3) (2005) 1118–1139.
- [18] A. Narayan, D. Xiu, Stochastic collocation methods on unstructured grids in high dimensions via interpolation, *SIAM J. Sci. Comput.* 34 (3) (2012) 1729–1752.
- [19] J. D. Jakeman, A. Narayan, T. Zhou, A generalized sampling and preconditioning scheme for sparse approximation of polynomial chaos expansions, *SIAM J. Sci. Comput.* 39 (3) (2017) 1114–1144.
- [20] L. Sirovich, Turbulence and the dynamics of coherent structures. I–III. *Quart. Appl. Math.* 45 (3) (1987) 561–590.
- [21] M. Frangos, Y. Marzouk, K. Willcox, B. van Bloemen Waanders, Surrogate and reduced-order modeling: A comparison of approaches for large-scale statistical inverse problems, *Large-Scale Inverse Problems and Quantification of Uncertainty*, Wiley Blackwell, 2010.
- [22] W. H. Schilders, H. A. van der Vorst, J. Rommes, *Model Order Reduction: Theory, Research Aspects and Applications*, Berlin: Springer, 2008.
- [23] P. Benner, S. Gugercin, K. Willcox, A survey of projection-based model reduction methods for parametric dynamical systems, *SIAM Rev.* 57 (4) (2015) 483–531.
- [24] D. H. Xiao, Non-intrusive reduced order models and their applications, PhD diss., PhD thesis, Imperial College London, 2016.
- [25] C. Audouze, F. D. Vuyst, P. B. Nair, Reduced-order modeling of parameterized PDEs using timespace-parameter principal component analysis, *Internat. J. Numer. Methods Eng.* 80 (8) (2009) 1025–1057.
- [26] D. Kosambi, Statistics in function space, *J. Indian Math. Soc.* 7 (1943) 76–88.
- [27] C. Audouze, F. D. Vuyst, P. B. Nair, Nonintrusive reduced-order modeling of parametrized time-dependent partial differential equations. *Numer. Methods for Partial Differ. Equ.* 29 (5) (2013) 1587–1628.
- [28] M. Xiao, P. Breikopf, R. F. Coelho, C. Knopf-Lenoir, M. Sidorkiewicz, P. Villon, Model reduction by CPOD and Kriging, *Struct. Multidiscip. O.* 41 (4) (2010) 555–574.
- [29] M. Guo, J. S. Hesthaven, Reduced order modeling for nonlinear structural analysis using Gaussian process regression, *Comput. Methods Appl. Mech. Eng.* 341 (2018) 807–826.
- [30] M. Guo, J. S. Hesthaven, Data-driven reduced order modeling for time-dependent problems, *Comput. Methods Appl. Mech. Eng.* 345 (2019) 75–99.
- [31] B. R. Noack, M. Morzynski, G. Tadmor, *Reduced-Order modelling for flow control*. Vol. 528, Springer Science & Business Media, 2011.
- [32] M. Vassile, M. Gunot, I. Lepot, C. Sainvitu, J. Goblet, R. Filomeno Coelho, Adaptive sampling strategies for non-intrusive POD-based surrogates, *Eng. Comput.* 30 (4) (2013) 521–547.
- [33] J. S. Hesthaven, S. Ubbiali, Non-intrusive reduced order modeling of nonlinear problems using neural networks, *J. Comput. Phys.* 363 (2018) 55–78.

- [34] Q. Wang, J. S. Hesthaven, D. Ray, Non-intrusive reduced order modeling of unsteady flows using artificial neural networks with application to a combustion problem, *J. Comput. Phys.* (2018).
- [35] R. Swischuketal, L. Mainini, B. Peherstorfer, Karen Willcox, Projection-based model reduction: Formulations for physics-based machine learning, *Comput. Fluids* (2018).
- [36] A. Doostan, R. Ghanem, J. Red-Horse, Stochastic model reduction for chaos representations, *Comput. Methods Appl. Mech. Eng.* 196 (37–40) (2007) 3951–3966.
- [37] M. Raisee, D. Kumar, C. Lacor, A non-intrusive model reduction approach for polynomial chaos expansion using proper orthogonal decomposition, *Internat. J. Numer. Meth. Eng.* 103 (4) (2015) 293–312.
- [38] D. Kumar, M. Raisee, C. Lacor, An efficient non-intrusive reduced basis model for high dimensional stochastic problems in CFD, *Comput. Fluids* 138 (2016) 67–82.
- [39] S. Abraham, P. Tsirikoglou, J. Miranda, C. Lacor, F. Contino, G. Ghorbaniasl, Spectral representation of stochastic field data using sparse polynomial chaos expansions, *J. Comput. Phys.* 367 (2018) 109–120.
- [40] A.M. De Gennaro, C. W. Rowley, L. Martinelli, Data-driven low-dimensional modeling and uncertainty quantification for airfoil icing, 3rd AIAA Applied Aerodynamics Conference, AIAA AVIATION Forum, AIAA 2015-3383.
- [41] M. Loeve, *Probability Theory*, fourth ed., Springer-Verlag, New York, 1977.
- [42] H. Hotelling, Analysis of a complex of statistical variables with principal components, *J. Educ. Psychology* 24 (6) (1933) 417–441.
- [43] I. Jolliffe, Principal component analysis, in *Encyclopedia of Statistics in Behavioral Science*, John Wiley & Sons, 2005.
- [44] V. Algazi, D. Sakrison, On the optimality of the Karhunen-Loève expansion. *IEEE Trans. Information Theory* 15 (2) (1969) 319–320.
- [45] P. Z. Qian, Nested Latin hypercube designs, *Biometrika* 96 (4) (2009) 957–970.
- [46] P. Holmes, J. L. Lumley, G. Berkooz, *Turbulence, Coherent Structures, Dynamical Systems and Symmetry*, Cambridge, New York, 1996.
- [47] S. Volkwein, *Model Reduction Using Proper Orthogonal Decomposition*, Lecture Notes, Faculty of Mathematics and Statistics, University of Konstanz, 2011.
- [48] B. Noble, *Applied Linear Algebra*, Englewood Cliffs, NJ : Prentice-Hall, 1969.
- [49] R. H. Cameron and W. T. Martin, The orthogonal development of non-linear functionals in series of Fourier-Hermite functionals, *Ann. Math.* 48 (2) (1947) 385–392.
- [50] O. G. Ernst, A. Mugler, H.-J. Starkloff, and E. Ullmann, On the convergence of generalized polynomial chaos expansions, *ESAIM: M2AN* 46 (2) (2012) 317–339.
- [51] S. Hosder, R.W. Walters, R. Perez, A non-intrusive polynomial chaos method for uncertainty propagation in CFD simulations, in: 44th AIAA Aerospace Sciences Meeting and Exhibit, AIAA-2006-891, Reno (NV), 2006.
- [52] S. Hosder, R. Walters, M. Balch, Efficient sampling for non-intrusive polynomial chaos applications with multiple input uncertain variables, in: 48th AIAA/ASME/ASCE/AHS/ASC Structures, Structural Dynamics, and Materials Conference, Honolulu, Hawaii, 2007.
- [53] A. Doostan, H. Owghadi, A non-adapted sparse approximation of PDEs with stochastic inputs, *J. Comput. Phys.* 230 (8) (2011) 3015–3034.
- [54] M. Berveiller, B. Sudret, M. Lemaire, Stochastic finite elements: a non intrusive approach by regression. *Eur. J. Comput. Mech.* 15 (1–3) (2006) 81–92.
- [55] R. Baptista, V. Stolbunov, P. B. Nair, Some greedy algorithms for sparse polynomial chaos expansions, *J. Comput. Phys.* 387 (2019) 303–325.
- [56] O. P. Le Maître, O. M. Knio, H. N. Najm, R. G. Ghanem, Uncertainty propagation using Wiener-Haar expansions, *J. Comput. Phys.* 197 (1) (2004) 28–57.
- [57] X. Wan, G. Karniadakis, An adaptive multi-element generalized polynomial chaos method for stochastic differential equations, *J. Comput. Phys.* 209 (2) (2005) 617–642.
- [58] X. Wan, G. Karniadakis, Beyond Wiener-Askey expansions: handling arbitrary PDFs, *J. Sci. Comput.* 27 (1) (2006) 455–464.
- [59] F. Nobile, R. Tempone, C. G. Webster, A sparse grid stochastic collocation method for partial differential equations with random input data, *SIAM J. Numer. Anal.* 46 (5) (2008) 2309–2345.
- [60] C. Wang, J.S. Hesthaven, J. Bai, Y. Zhang, T. Yang, Greedy non-intrusive reduced order model for fluid dynamics, *AIAA J.* 56 (12) (2018)

4927–4943.

- [61] R. E. Caflisch, Monte carlo and quasi-monte carlo methods, *Acta Numer.* 7 (1998)1–49.
- [62] E. Novak, K. Ritter, High dimensional integration of smooth functions over cubes, *Numer. Math.* 75 (1) (1996) 79–97.
- [63] S. Marelli, B. Sudret, UQLab user manual - Polynomial Chaos Expansions, Report UQLab-V1.1-104, Chair of Risk, Safety & Uncertainty Quantification, ETH Zurich, 2018.
- [64] O. P. Le Maître, M. Reagan, H. N. Najm, R. G. Ghanem, O. M. Knio, A stochastic projection method for fluid flow. II: Random process, *J. Comput. Phys.* 181 (2002) 9–44.
- [65] J. Peng, J. Hampton, A. Doostan, A weighted l_1 -minimization approach for sparse polynomial chaos expansions, *J. Comput. Phys.* 267 (2014) 92–111.
- [66] J. Hampton, A. Doostan, Basis adaptive sample efficient polynomial chaos (BASE-PC), *J. Comput. Phys.* 371 (2018) 20–49.
- [67] X. Pan, K. Kim, C. Lee, J.-I. Choi, A decoupled monolithic projection method for natural convection problems, *J. Comput. Phys.* 314 (2016) 160–166.
- [68] X. Pan, K. Kim, C. Lee, J.-I. Choi, Fully decoupled monolithic projection method for natural convection problems, *J. Comput. Phys.* 334 (2017) 582–606.
- [69] X. Pan, K. Kim, C. Lee, J.-I. Choi, Efficient monolithic projection method for time-dependent conjugate heat transfer problems, *J. Comput. Phys.* 369 (2018) 191–208.